Ultramicroscopy 257 (2024) 113891

Contents lists available at ScienceDirect

Ultramicroscopy

journal homepage: www.elsevier.com/locate/ultramic

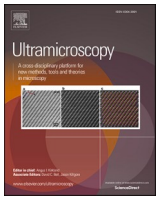

Noise-dependent bias in quantitative STEM-EMCD experiments revealed by bootstrapping

Hasan Ali [a,b,e,*], Jan Rusz [c], Daniel E. Bürgler [d], Roman Adam [d], Claus M. Schneider [d], Cheuk-Wai Tai [b], Thomas Thersleff [b]

[a] Department of Materials Science and Engineering, Uppsala University, Box 534, Uppsala 751 21, Sweden
[b] Department of Materials and Environmental Chemistry, Stockholm University, Stockholm 106 91, Sweden
[c] Department of Physics and Astronomy, Uppsala University, Box 516, Uppsala 751 20, Sweden
[d] Peter Grünberg Institut, Forschungszentrum Jülich GmbH, Jülich D-52425, Germany
[e] Ernst Ruska-Centre for Microscopy and Spectroscopy with Electrons, Forschungszentrum Jülich, Jülich 52425, Germany

ARTICLE INFO

Keywords:
Electron magnetic circular dichroism
Electron energy loss spectroscopy
Scanning
Transmission electron microscopy
Bootstrapping
Noise dependent bias
Error analysis

ABSTRACT

Electron magnetic circular dichroism (EMCD) is a powerful technique for estimating element-specific magnetic moments of materials on nanoscale with the potential to reach atomic resolution in transmission electron microscopes. However, the fundamentally weak EMCD signal strength complicates quantification of magnetic moments, as this requires very high precision, especially in the denominator of the sum rules. Here, we employ a statistical resampling technique known as bootstrapping to an experimental EMCD dataset to produce an empirical estimate of the noise-dependent error distribution resulting from application of EMCD sum rules to bcc iron in a 3-beam orientation. We observe clear experimental evidence that noisy EMCD signals preferentially bias the estimation of magnetic moments, further supporting this with error distributions produced by Monte-Carlo simulations. Finally, we propose guidelines for the recognition and minimization of this bias in the estimation of magnetic moments.

1. Introduction

Electron magnetic circular dichroism (EMCD) [1] is a transmission electron microscopy (TEM) technique that utilizes electron energy loss spectroscopy (EELS) to measure the element-specific magnetic moments of ferro- or ferrimagnetic materials. EMCD is the electron equivalent of the well-established X-ray based technique x-ray magnetic circular dichroism XMCD [2], with the key difference that the conjugated momentum transfer relies on the crystal splitting in EMCD rather than a circularly-polarized radiation source. While EMCD can measure the element specific magnetic moments of the materials, it also offers the highest possible spatial resolution [3–6] with sufficient depth of analysis, something which is not possible with XMCD and other techniques due to either limited spatial resolution [7,8] or insufficient depth resolution [9,10]. Recently, differential phase contrast (DPC) microscopy has achieved atomic resolution magnetic measurements [11] but this requires a TEM with a custom-designed objective lens system [12] to obtain atomic resolution electron probes at the specimen under magnetic field free environment. Additionally, DPC lacks the ability to quantify spin and orbital magnetic moments, while these critical properties can be extracted from EMCD experiments through application of EMCD sum rules [13]. A comprehensive review on EMCD can be found here [14].

Although EMCD comes with many attractive advantages over the complementary techniques for magnetic characterization, its hallmark feature – the quantitative estimation of orbital and spin magnetic moments – is particularly challenging. As initially described by Schattschneider et al. [1], an EMCD signal is experimentally obtained by taking the difference of EELS spectra acquired at conjugated scattering angles across the diffracted spots in the reciprocal space. In practice, these scattering angles lie at off-axis positions far away from the Bragg spots, yielding a signal that can be orders of magnitude smaller than standard EELS experiments, thereby resulting in a notoriously low signal to noise ratio (SNR). While this design is sufficient to reveal modifications to the selection rules governing 2p to 3d transitions in transition metals caused by the presence of an uncompensated magnetic field, a quantitative estimation of magnetic moments requires application of the EMCD sum rules [13,15]. This involves significant signal processing steps including

* Corresponding author at: Department of Materials Science and Engineering, Uppsala University, Box 534, Uppsala 751 21, Sweden.
E-mail address: ali.hasan@angstrom.uu.se (H. Ali).

https://doi.org/10.1016/j.ultramic.2023.113891
Received 7 July 2023; Received in revised form 13 November 2023; Accepted 23 November 2023
Available online 24 November 2023

deconvolution [16], continuum removal (typically achieved by subtracting two conjugated signals under the assumption of ideal symmetrical scattering conditions), integration, and numerical manipulation, with each additional processing step introducing additional errors to the already noisy signal. Since the ratio of magnetic orbital to spin moments (m_L/m_S) is very small for most of the technologically important magnetic materials, minor errors in the quantification process risk interpretation as novel magnetic properties. Despite many efforts to improve the EMCD signal strength [16–20] poor SNR remains a major challenge for wider adoption of the EMCD method.

Although the influence and analysis of statistical errors is extremely important in EMCD experiments, most published studies reporting error bars have derived them independently using individualized approaches [3,5,21–24]. These studies either estimate statistical errors from a very small sample size [5], or they analytically derive them for single EMCD spectra, typically using residuals in the pre-edge or post-edge region of the EELS spectra as estimators for the statistical variance, and then propagating them accordingly [6,20,25–28]. While this may be appropriate given the small number of studies and individual spectra available to scientists at the time of publication, it can also be viewed as problematic from the perspective of the wider community for the following reasons. These approaches all implicitly assume that the errors follow a normal distribution centered on the calculated value, and that this distribution function does not change as a function of the initial noise corruption of the original data. These assumptions have not yet been substantiated with supportive evidence and, thus, should be publicly challenged, especially considering the complicated procedure required to apply the sum rules. Moreover, the errors determined in many EMCD papers [5,6,23,24,26,29,30] are comparable to XMCD experiments [31, 32] despite the latter technique boasting a significantly higher SNR.

One way to challenge the validity of the assumptions used to justify the analytical, theory-centric derivation of statistical errors outlined in the papers above is to take an empirical experiment-centric approach. In principle, such an empirical approach could be achieved by independently measuring m_L/m_S many thousands of times from the exact same region of material under a range of different SNR conditions. Multiple measurements at a given SNR could then be fit to a distribution function to provide a more complete description of statistical errors (also subverting the need to worry about systematic errors), while different SNR values could reveal any noise-dependent variations to this distribution function. However, in practice, this experimental design is greatly complicated by the highly localized nature of EMCD itself as well as the high radiation dose needed for such experiments. Extracting the EMCD signal from exactly the same region of the sample for the time necessary for this experiment would inevitably lead to time-dependent beam damage problems in even the most radiation-robust samples. Also, if a large, parallel probe is used, exposing fresh sample regions for each measurement introduces the prospect of systematic errors arising from variations due to crystal tilt [25] and sample thickness [33], in addition to placing unreasonably large burden on the homogeneity of the sample preparation and growth. Thus, the experimental design needed to achieve the ideal conditions to take the empirical approach is time and cost prohibitive.

In this paper, we argue that, by combining recent advances in EMCD experimental design with a well-established statistical inference procedure broadly known as bootstrapping, we can approximate the conditions needed for an empirical error analysis reasonably closely, thereby allowing us to study and discuss the aptness of the aforementioned assumptions. The experimental design we employ is known as STEM-EMCD and has been described previously [3], while bootstrapping is a resampling-with-replacement technique commonly used to estimate the statistical error distribution from sample-limited datasets [34]. Although bootstrapping has previously been applied to various electron microscopy experiments [35–37], its use in this experiment specifically allows us to test the dependence of the error distribution shape on the SNR of EMCD signal, which has not yet been investigated. Critically, we observe that one of the main assumptions justifying the analytical approach to error analysis – that of symmetric, normally-distributed errors – is not appropriate for lower SNR values. This leads to an obvious noise-dependent bias towards higher values of m_L/m_S that can have major ramifications for the most high-impact studies, where signal is at an absolute premium and high SNR may simply be infeasible. Moreover, from the Monte-Carlo simulations, we find that this noise dependent bias is also material dependent and for the same noise levels, materials having larger values of m_L/m_S show higher bias. Importantly, the approach we outline here provides us with sufficient information to mathematically describe and account for this bias, permitting us to propose cautionary guidelines for the interpretation of future quantitative EMCD results. The methods and workflow proposed here are also transferrable to other magnetic materials and can be generalized to other STEM-based experiments or even XMCD error analysis under the right conditions.

2. Methods

2.1. Sample fabrication

The sample used in this experiment was fabricated in the same way as in [38]. The fabrication was carried out by thermally evaporating a 40 nm thick bcc-Fe layer and a 3 nm thick Al top layer onto a 5 nm thick Si_3N_4 membrane under ultra-high vacuum conditions. The membrane was used without prior cleaning and kept at room temperature during deposition. The layer thicknesses were monitored with calibrated quartz microbalances and are estimated to fluctuate by about 3 %. To achieve larger lateral Fe grain sizes exceeding 100 nm, the Fe film was annealed immediately after deposition for 2 h at 750 °C. Subsequently, the Al cap layer was deposited at room temperature to protect the Fe from oxidation upon exposure to air.

2.2. STEM EMCD

To apply the bootstrapping technique on the EMCD analysis, the STEM-EMCD technique was employed [39–43] using a convergence semi-angle of 8.0 mrad at 300 kV. The experiments were performed on Thermo Fisher Themis-Z with a probe and image corrector and equipped with a Gatan Quantum imaging filter. First, a thin single-crystalline grain of iron was identified and tilted to the three-beam condition having the set of systematic row vectors $g = \langle 002 \rangle$. The grain itself was specifically chosen to be relatively featureless to facilitate a similar EMCD signal from each pixel position. Tilting was performed manually by inspecting the CBED pattern from a region adjacent to the ROI. The ROI as well as a corresponding CBED pattern are provided in Fig. 1(a). Considering the sensitivity of EMCD signal to thickness and orientation changes, special care was taken to choose the area of analysis with minimum changes in these factors. Moreover, the EMCD experiment was performed in 3-beam orientation instead of 2-beam orientation as it helps to counter variation of EMCD signal due to small residual orientation changes and minimizes the errors arising due to post-edge normalization of the spectra [43].

Once the diffraction conditions were configured, the magnification of the projector system was adjusted to yield an EELS collection semi-angle of 7 mrad at the 2.5 mm spectrometer entrance aperture. A new Cartesian coordinate system was established in which the centres of the 000 and 002 Bragg disks were defined as $x_0, y_0 = [0, 0]$ and $x_g, y_g = [1, 0]$ using a custom written script. Thus, x describes the direction along the systematic row vector while y describes the orthogonal direction, with the units for both normalized to 13.7 mrad (the scattering angle of Fe (002) lattice planes at 300 kV). Four chiral positions were set in this coordinate system following all sign permutations of the coordinates x_{ij}, $y_{ij} = [\pm 0.5, \pm 0.9]$. These positions are labelled according to their sign combination as shown in Fig. 1(a).

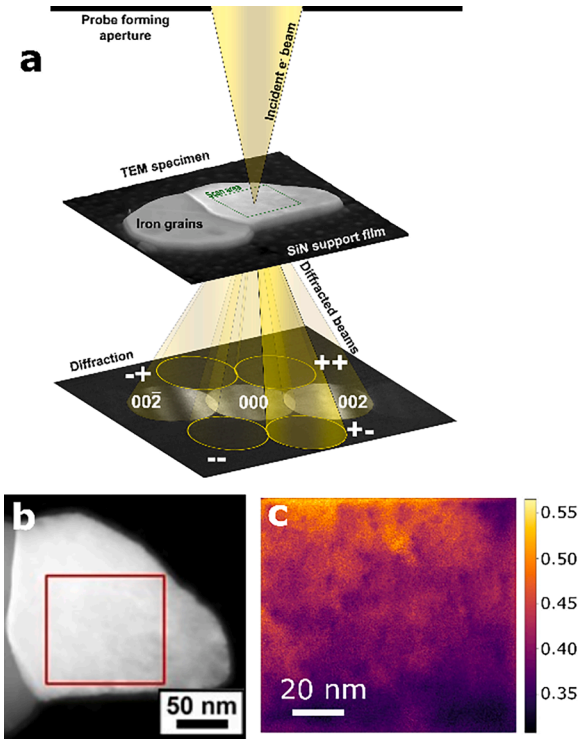

Fig. 1. (a) A schematic showing the STEM-EMCD experimental setup, a fine electron probe is raster scanned across a well-defined region of the sample and an EELS spectrum is acquired at each probe position. The process is repeated four times, for the four aperture positions shown in the diffraction plane. The STEM-HAADF image and the diffraction pattern are taken from the real experimental data (b) HAADF image showing the area of the specimen scanned in the STEM-EMCD experiment (c) Thickness map for the scanned area extracted from low-loss EELS dataset. The colour bar shows the t/λ values.

A total of five EELS Spectrum Images (ESI) were acquired, defined here as $S_{(x,y)}$. Each $S_{(x,y)}$ is acquired as a mode-3 tensor having dimensions $N_e \times N_y \times N_x$ where N_e represents the number of energy channels and N_x and N_y represent the number of probe positions (or pixels) in the x and y directions and whose content is defined by its aperture position x_{ij}, y_{ij} (see Fig. 1). An ROI measuring 114.0×104.5 nm was defined with a step size of 0.38 nm (denoted in Fig. 1(b)), such that $N_x = 300$ and $N_y = 275$. Prior to each scan, the initial probe position was corrected using a survey image that was acquired with the HAADF detector at the outset of the experiment, thereby ensuring a reasonable spatial registration between scans at this resolution. The collection angles for each scan were set by using the diffraction shift deflectors to offset the diffraction pattern onto the spectrometer entrance aperture according to the x, y convention for chiral positions established above. The ROI was scanned a total of 5 times in the order "++", "+-", "-+", "--", "00". The final scan ("00") was performed on-axis and was used to acquire the low-loss EELS dataset to allow for deconvolution as well as to estimate the region thickness, which is presented in Fig. 1(c). The spectrometer contains 2048 energy channels ($N_e = 2048$) and was configured using a dispersion of 0.25 eV / channel and an offset of 400 eV, allowing for both the iron and oxygen edges to be captured. During acquisition, the drift tube was excited using a sawtooth waveform to continuously shift the recording position of the EEL spectrum on the spectrometer scintillator, a technique known as gain averaging [44]. The dwell time for each spectrum was 5 ms and a high quality gain reference was acquired for each data-cube post-acquisition [45].

2.3. Pre-processing of STEM-EMCD data

Pre-processing of the STEM-EMCD data was performed following the procedure outlined in Thersleff et al. [38]. First, strong pixel-level outliers were removed. Second, all $S_{(x,y)}$ were concatenated along their y-axis direction. An EELS spectrum from the first dataset was chosen and used a reference to which all other spectra were aligned using cross-correlation. The shift correction roughly followed the sawtooth waveform used for the gain averaging and any outliers were corrected using this. Finally, the $S_{(x,y)}$ datasets corresponding to conjugate aperture positions were summed elementwise, yielding $S_+ = S_{++} + S_{--}$ and $S_- = S_{+-} + S_{-+}$ where the + and – subscripts refer to the sign of their corresponding aperture positions defined above.

2.4. Bootstrapping workflow

STEM-EMCD is primarily advantageous in that it fractionates the beam dose over the scanning region. Integration of all recorded spectra within each chiral EELS spectrum image (ESI) datacube subsequently maximizes the SNR of the resulting EMCD while minimizing the influence of beam damage. However, it also means that each ESI can be subsampled to estimate lower SNR values. We take advantage of this property to study the SNR dependence of statistical EMCD errors here with bootstrapping.

The two chiral ESI datasets (S_+ and S_-) were unfolded along their spatial sampling dimension to matrices having dimensions $N_e \times N_{\text{px}}$ where $N_{\text{px}} = N_x \cdot N_y$. We now define a subsampling parameter N_s, also called "specsum," which denotes the number of spectra that are integrated for each bootstrapping iteration. N_s roughly corresponds to a SNR value, with the maximum SNR occurring when $N_s = N_{\text{px}}$. N_s serves to subsample the original ESI datacube, simulating the situation where the number of pixels in an experiment would be less than N_{px}. Bootstrapping in this manuscript involves iterating this subsampling action N times for each N_s where N_s pixel indices are chosen at random with replacement, meaning that it is possible for the same pixel to be chosen zero or multiple times for a given iteration. The subsampling indices for any given iteration n can be summarized as an integer matrix I_n having dimensions $N_y \times N_x$ where the value of each pixel is simply the number of times that particular spectrum should be counted (see Fig. 2 for examples). I_n is subsequently unfolded into a $N_{\text{px}} \times 1$ vector.

At each specsum interval N_s, a total of $N = 1000$ bootstrapping iterations where performed. For any given bootstrapping iteration n, the two spectra corresponding to the integration over the randomly chosen pixels in I_n were extracted by taking the outer product between it and $S_\pm$.

$$f_{\pm,n} = S_\pm I_n \tag{1}$$

In this notation, $f_{\pm,n}$ denotes the two integrated chiral spectra (f_+ and f_-, both being $N_e \times 1$ vectors) at bootstrapping index n from which an EMCD signal was extracted and m_L/m_S was calculated. This process is illustrated for clarity in Fig. 2. Each column denotes a chosen value of N_s(specsum), while each row shows a bootstrapping sample n for that N_s. The maps depict I_n, which is a 2D array of the selected indices used for summation. As can be seen, the same index can be selected multiple times, which is graphically represented as a color denoted by the corresponding colorbar. The resulting $f_\pm$ combination reveals a corresponding EMCD signal, extracted using the methods described above. This is used to take a single estimate of m_L/m_S. The full population of 1000 estimates for each specsum is visualized in the final row in the form of a 1D histogram and was fit to an epsilon skew-normal distribution function to reliably estimate the distribution of errors in m_L/m_S for that given SNR.

3. Results

We produce various SNR conditions for EMCD analysis by integrating different number of raw EELS spectra (specsum). The application of bootstrapping workflow as described above on the experimental ESI datasets produces 1000 EMCD signals for each value of SNR (specsum)

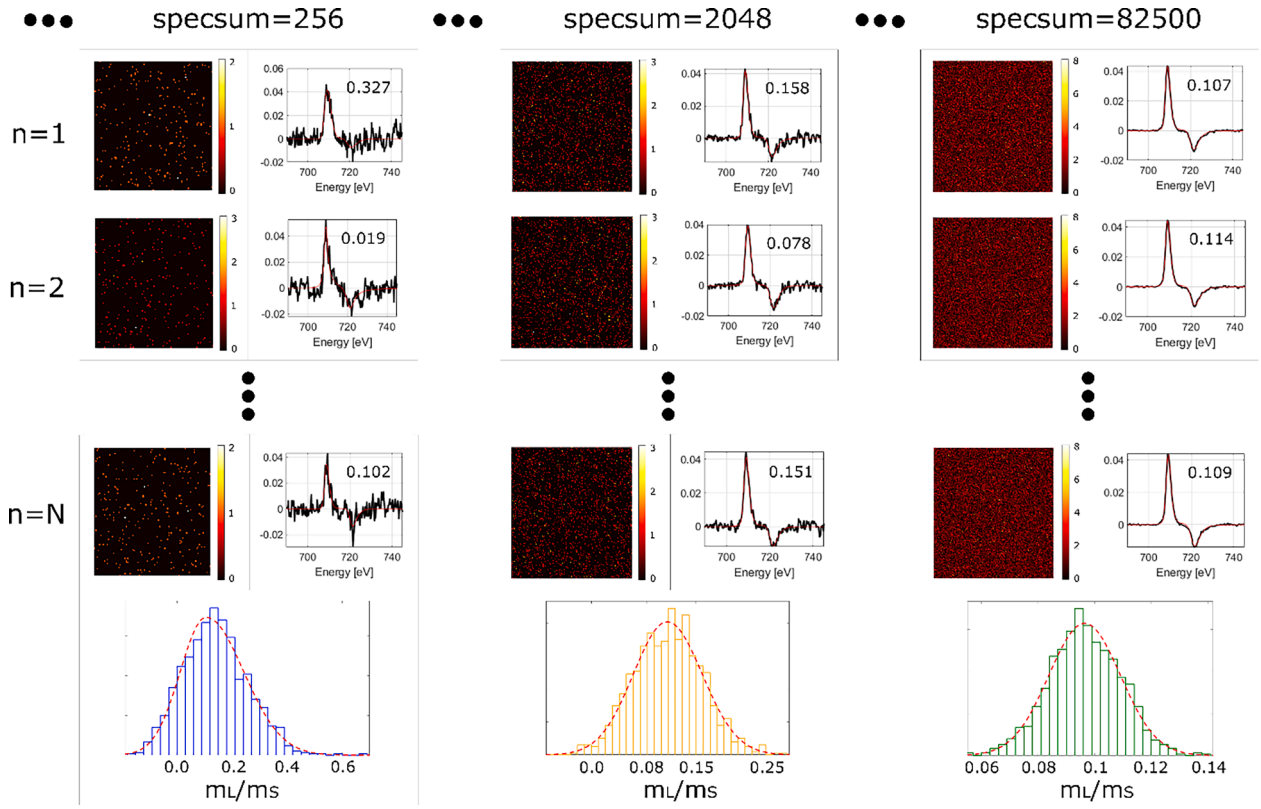

Fig. 2. An illustration of bootstrapping workflow. For each value of N_s (called specsum here), the spectra are randomly chosen and summed up from the chiral ESI datasets and the EMCD signal is obtained by processing and subtracting these spectra. The procedure is repeated for $N = 1000$ times. The histograms show the distribution of the obtained 1000 m_L/m_S values for each value of specsum.

which is determined for both L_3 and L_2 energy loss edges of Fe. The EMCD signals are subsequently passed through the quantification workflow described in Ref. [38] to obtain the corresponding m_L/m_S values. Consequently, we have a dataset where for each SNR value, we have a distribution of 1000 m_L/m_S values. The best way to visualize all these distributions as a function of SNR is a violin plot. In such a plot, each distribution is represented as a violin where the mean and median of each distribution are presented by a bar and a dot respectively. The height of each violin indicates the dispersion in each dataset as shown in Fig. 3.

The first and obvious observation from Fig. 3 is that the dispersion in the resulting m_L/m_S values gets higher as the SNR of the EMCD signal

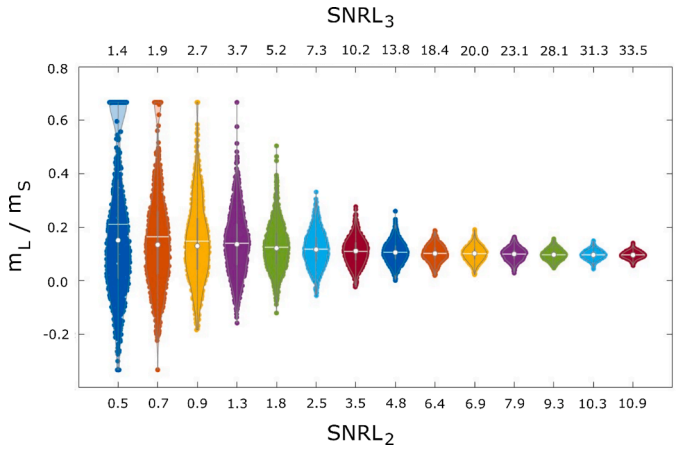

Fig. 3. A violin plot showing the distribution of m_L/m_S values as a function of signal to noise ratio at L_3 and L_2 energy loss edges. The white bar and dot in each violin indicate the mean and median of the distribution.

gets lower. The mean value of m_L/m_S for each SNR is indicated by a white bar in each distribution. It is worth noting that the error bars which can be estimated by the height of each violin seem to be much higher than the typical error bars reported in EMCD literature and approach $\pm$ 0.5 for EMCD signals with low SNRs, which is about 5 times the typical m_L/m_S value for bcc Fe. Such large errors can easily mislead quantification results for low SNR

Another assumption made in the EMCD experiments is that the error bars are symmetrical and follow a normal distribution around the mean value measured in any experiment. While fitting the m_L/m_S distributions shown in Fig. 3, we find that a simple normal distribution function fails to fit the histograms as the SNR value decreases. By carefully fitting different probability distribution functions (PDF) to the results, we find that an epsilon skew-normal distribution (ESD) [46] fits best to the results and it can be clearly seen in the left most fitted histogram in Fig. 2. The ESD belongs to the family of asymmetric distribution functions consisting of a location (θ), scale (σ) and skewness (ε) parameter, and it reduces to the normal distribution when $\varepsilon = 0$. This noise dependent skewness is also reflected in the mean m_L/m_S value for each distribution and biases the mean to larger values as shown in Fig. 3. It means that the m_L/m_S values would presumably tend to be higher than the real values for noisy EMCD signals.

Considering that the quantitative EMCD analysis is carried out by taking the ratio of the summation/differences seen at L_3 and L_2 edges (Eq. (1)), one of the reasons for this noise-dependent bias in the resulting m_L/m_S values can be the asymmetric degradation of EMCD signal at L_3 and L_2 edges. The relatively lower signal seen at L_2 compared to L_3 edge causes a higher and quicker degradation of $SNRL_2$ than $SNRL_3$ for the same noise levels. It is also evident from Fig. 3 that the $SNRL_2$ is much lower than $SNRL_3$ for the same EMCD signals. Furthermore, the L_2 energy loss edge is usually broader than the L_3 edge, spreading over more channels on the CCD, accumulating more readout noise, resulting in

faster deterioration of L_2 EMCD signal. Looking at the violin plots shown in Fig. 3, it appears that a simple median gives a closer estimate of the m_L/m_S as compared to the mean and this gets pronounced for lower SNR values. For the EMCD signals with the highest and lowest SNR in Fig. 3, the mean m_L/m_S value changes from 0.095 to 0.21 whereas the change in median value is from 0.096 to 0.15 which suggests that using a median value for weaker EMCD signals can give a better prediction of m_L/m_S. To verify and support our experimental observations, we carried out Monte-Carlo simulations described below.

The error distribution for m_L/m_S can be empirically determined using a Monte Carlo approach, which is described here. We begin by restating the sum rules [13,47]:

$$\frac{m_L}{m_S} = \frac{2}{3}\frac{\int_{L_3}\Delta\sigma(E)\mathrm{d}E + \int_{L_2}\Delta\sigma(E)\mathrm{d}E}{\int_{L_3}\Delta\sigma(E)\mathrm{d}E - 2\int_{L_2}\Delta\sigma(E)\mathrm{d}E} \tag{2}$$

As shown in Muto et al. [48], Eq. (2) can be simplified by taking the full integral of the EMCD signal. This results in Eq. (3) where p and q are defined in Fig. 4.

$$\frac{m_L}{m_S} = \frac{2q}{9p - 6q} \tag{3}$$

As in Muto et al. [48], we adopt Eq. (3) and set $p = 1$, allowing m_L/m_S to act as a function of q alone. We now assume a variable amount of uncertainty on the estimate of q, which we can be defined as a percentage of unity, as p has been normalized to 1.

First, we use Monte Carlo simulations to simulate the error distribution for a given material, which we define as having a "true" $m_L/m_S = 0.05$, corresponding to the case where $q = 0.8p$. We then assume that the experimental errors in estimating q can be modeled as arising from a normal distribution having an expected value of 0.05 and a standard deviation σ_q that varies depending on the noise level of the experiment. Again, σ_q is defined as a percentage of unity for simplicity. Here, we simulate cases where σ_q ranges from 5 % to 40 %. For each σ_q, we draw 1000 random samples (q_i) from this distribution given the corresponding σ_q. Each q_i is converted into an observed m_L/m_S using Eq. (3) and the results for all σ_q are summarized in Fig. 5.

In Fig. 5(a), we observe that, despite assuming a normal distribution of errors on q, the retrieved distribution of m_L/m_S values is asymmetrical and strongly skewed to higher values. While this is not very pronounced for lower σ_q, it becomes increasingly significant as the estimate of q becomes more uncertain. As described in the experimental results, a normal distribution function does not adequately model this empirical distribution, and its use may result in an estimate of m_L/m_S that is biased towards larger values for higher σ_q. We therefore use an epsilon skew normal distribution (ESD) introduced above. The three ESD PDF models for these data are provided as solid lines in Fig. 5(a). To visualize the influence of the bias in these data, we use a violin plot, presented in Fig. 5(b). The colored bars show the mean values whereas the dots show the median of each dataset. Like the experimental observations, a simple median predicts the true m_L/m_S for this material much better than the mean, and that this is most pronounced for the case when the uncertainty in q is highest.

We now consider the case where the experimental uncertainty is constant but three different materials are measured, with $m_L/m_S = 0.38$, 0.17, and 0.05 for materials A, B, and C, respectively. For each material, we assume $\sigma_q = 0.10$ and use the same Monte Carlo approach described above to estimate the material-specific error distribution.

The results of this analysis are presented in Fig 6. When the true value of $m_L/m_S = 0.05$, we observe that both the ESD skew and scale are relatively low. However, for higher m_L/m_S, both of these parameters increase markedly. This finding underscores the need for very high SNR experiments when the true value of m_L/m_S is unknown but could potentially be somewhat large, as such materials will inherently carry a higher uncertainty in the estimation of their m_L/m_S values.

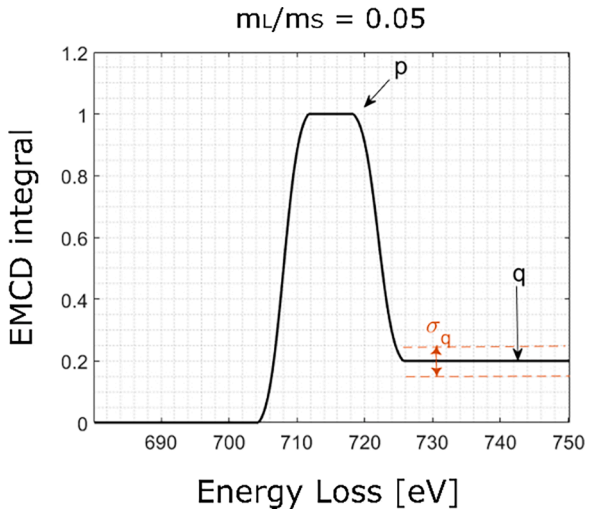

Fig. 4. An integral of the EMCD signal showing the p and q values used in Eq. (3).

4. Discussion

An EMCD signal is characterized by intensity differences observed at L_3 and L_2 energy loss edges in the EELS spectra of transition metals. The relatively blurred profile and inherently lower signal at L_2 energy loss edge makes it more challenging to experimentally retrieve the L_2 EMCD signal. This is evident from many experimental studies where the L_2 EMCD signal is either very weak or just disappears under the noise level [4,26,27,49,50]. While this is appropriate for a qualitative study, the quantitative analysis requires the detection of a clear signal at both L_3 and L_2 edges with sufficient SNR. As confirmed by both the experimental results and simulations shown above, for the noisy signals which are common to most EMCD experiments, the errors in quantification are not symmetric while considering the mean as the reported value and they are strongly skewed towards larger values, suggesting asymmetric error bars. It is important to note that this asymmetry in the error bars is mainly dependent on the $SNRL_2$ which means a higher SNR at L_3 edge does not guarantee a reliable quantitative result. So, we suggest taking $SNRL_2$ as the criterion to determine the reliability of quantification. We have plotted the skewness in m_L/m_S distributions obtained from the experimental data as a function of $SNRL_2$ in Fig 7. For $SNRL_2 > 5$ threshold, the error bars are symmetric, and the results follow a normal distribution. This threshold is similar as defined by rose criterion [51] which states that a signal must be 5 standard deviations above the background for a reliable detection. In practice, it is challenging to achieve this SNR, particularly at L_2 edge. If the experiment is done in TEM mode where one or few spectra are acquired, there is a fair possibility to get an over-estimated m_L/m_S value as a result of quantification unless the signal fulfils the criterion defined above. A better approach is to take multiple samples as done in a STEM-EMCD experiment. In this way, not only the electron dose can be efficiently distributed over the region of analysis, but a high SNR can be obtained by integrating multiple spectra in the dataset. If the quantitative process is run on individual spectra, the median of multiple measurements should be considered as the reference value as it gives a close estimate to the true m_L/m_S value. Moreover, the slope of the q segment in the EMCD integral shown in Fig. 4 can be very non-linear due to multiple effects such as correlated noise and fixed pattern noise, producing further uncertainties in quantification. We suggest using gain averaging [44] during acquisition to remove these artefacts.

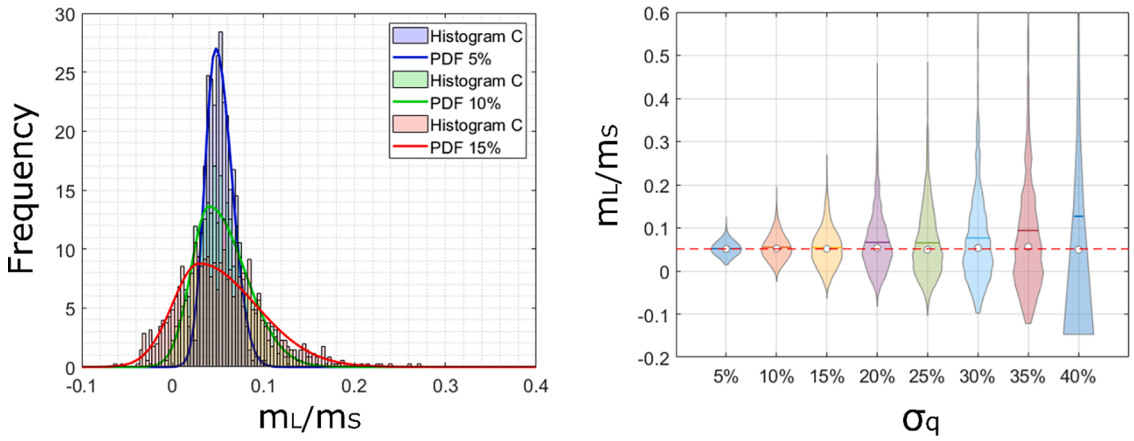

Fig. 5. Left: Histograms with fitted distribution functions showing the m_L/m_S values for the same material (here called 'C') with different noise characteristics, right: Violin plot showing the distribution of m_L/m_S for various noise levels.

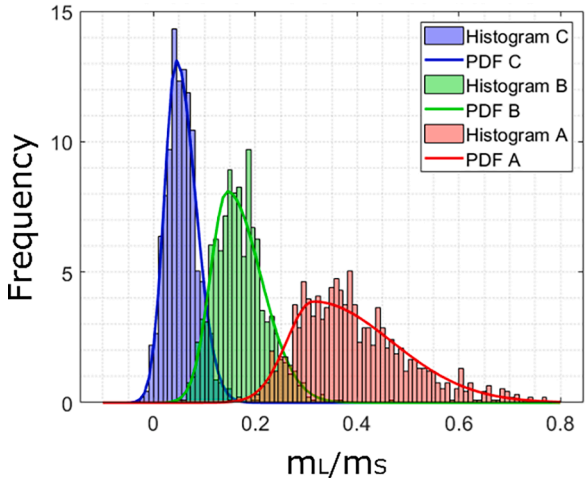

Fig. 6. Histograms fitted with distribution functions showing the m_L/m_S values for three different materials, considering the same noise characteristics.

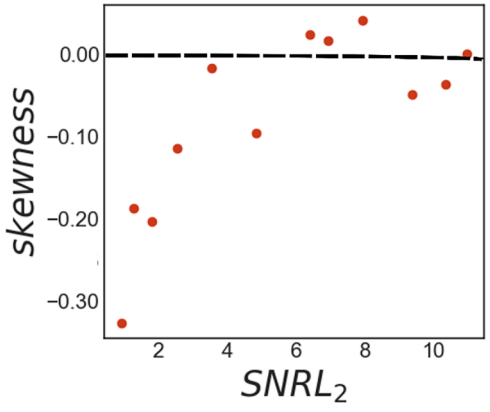

Fig. 7. Skewness in the distribution of m_L/m_S values plotted against SNR of L_2 for the experimental data.

5. Conclusions

We have employed bootstrapping to estimate errors in quantitative STEM-EMCD experiments. We report that the resulting m_L/m_S values are biased towards larger values for noisy signals. This bias is not only dependent on noise but also material dependent and the materials having larger intrinsic m_L/m_S values show higher bias for the same noise levels. The skewness in the distribution of resulting m_L/m_S values suggest using an asymmetric error bar for noisy signals whereas for multiple measurements, a median closely represents the true value.

Declaration of Competing Interest

The authors declare that they have no known competing financial interests or personal relationships that could have appeared to influence the work reported in this paper.

Data availability

Data will be made available on request.

Acknowledgments

H.A. acknowledges funding from Swedish Research Council (project nr. 2021–06748). H.A, C-W.T and T.T acknowledge the financial support from Swedish Foundation for Strategic Research SSF (ITM17–0301). T.T acknowledges Swedish Research Council (project nr. 2016–05113). J.R. acknowledges Swedish Research Council (project no.2021–03848), Carl Tryggers Foundation and STINT for financial support.

References

[1] P. Schattschneider, S. Rubino, C. Hébert, J. Rusz, J. Kuneš, P. Novák, E. Carlino, M. Fabrizioli, G. Panaccione, G. Rossi, Detection of magnetic circular dichroism using a transmission electron microscope, Nature 441 (2006) 486.
[2] T. Funk, A. Deb, S.J. George, H. Wang, S.P. Cramer, X-ray magnetic circular dichroism—a high energy probe of magnetic properties, Coord. Chem. Rev. 249 (2005) 3.
[3] T. Thersleff, J. Rusz, B. Hjörvarsson, K. Leifer, Detection of magnetic circular dichroism with subnanometer convergent electron beams, Phys. Rev. B 94 (2016), 134430.
[4] J. Rusz, S. Muto, J. Spiegelberg, R. Adam, K. Tatsumi, D.E. Bürgler, P.M. Oppeneer, C.M. Schneider, Magnetic measurements with atomic-plane resolution, Nat. Commun. 7 (2016) 12672.
[5] Z. Wang, et al., Atomic scale imaging of magnetic circular dichroism by achromatic electron microscopy, Nat. Mater. 17 (2018) 221, 2018 17:3.
[6] H. Ali, D. Negi, T. Warnatz, B. Hjörvarsson, J. Rusz, K. Leifer, Atomic resolution energy-loss magnetic chiral dichroism measurements enabled by patterned apertures, Phys. Rev. Res. 2 (2020), 023330.
[7] W. Chao, B.D. Harteneck, J.A. Liddle, E.H. Anderson, D.T. Attwood, Soft X-ray microscopy at a spatial resolution better than 15 Nm, Nature 435 (2005) 1210.
[8] P.A. Midgley, R.E. Dunin-Borkowski, Electron tomography and holography in materials science, Nat. Mater. 8 (2009) 271, 2009 8:4.
[9] S. Heinze, M. Bode, A. Kubetzka, O. Pietzsch, X. Nie, S. Blügel, R. Wiesendanger, Real-space imaging of two-dimensional antiferromagnetism on the atomic scale, Science (1979) 288 (2000) 1805.

[10] U. Kaiser, A. Schwarz, R. Wiesendanger, Magnetic exchange force microscopy with atomic resolution, Nature 446 (2007) 522, 2006 446:7135.
[11] Y. Kohno, T. Seki, S.D. Findlay, Y. Ikuhara, N. Shibata, Real-space visualization of intrinsic magnetic fields of an antiferromagnet, Nature 602 (2022) 234, 2022 602: 7896.
[12] N. Shibata, Y. Kohno, A. Nakamura, S. Morishita, T. Seki, A. Kumamoto, H. Sawada, T. Matsumoto, S.D. Findlay, Y. Ikuhara, Atomic resolution electron microscopy in a magnetic field free environment, Nat. Commun. 10 (2019) 1, 2019 10:1.
[13] L. Calmels, F. Houdellier, B. Warot-Fonrose, C. Gatel, M.J. Hÿtch, V. Serin, E. Snoeck, P. Schattschneider, Experimental application of sum rules for electron energy loss magnetic chiral dichroism, Phys. Rev. B 76 (2007) 60409.
[14] D. Song, Z. Wang, J. Zhu, Magnetic measurement by electron magnetic circular dichroism in the transmission electron microscope, Ultramicroscopy 201 (2019) 1.
[15] J. Rusz, O. Eriksson, P. Novák, P.M. Oppeneer, Sum rules for electron energy loss near edge spectra, Phys. Rev. B 76 (2007), 060408.
[16] H. Lidbaum, J. Rusz, A. Liebig, B. Hjörvarsson, P.M. Oppeneer, E. Coronel, O. Eriksson, K. Leifer, Quantitative magnetic information from reciprocal space maps in transmission electron microscopy, Phys. Rev. Lett. 102 (2009) 1.
[17] K. Tatsumi, S. Muto, J. Rusz, T. Kudo, S. Arai, Signal enhancement of electron magnetic circular dichroism by ultra-high-voltage TEM, toward quantitative nano-magnetism measurements, Microscopy 63 (2014) 243.
[18] H. Ali, T. Warnatz, L. Xie, B. Hjörvarsson, K. Leifer, Quantitative EMCD by use of a double aperture for simultaneous acquisition of EELS, Ultramicroscopy 196 (2019) 192.
[19] J. Verbeeck, C. Hébert, S. Rubino, P. Novák, J. Rusz, F. Houdellier, C. Gatel, P. Schattschneider, Optimal aperture sizes and positions for EMCD experiments, Ultramicroscopy 108 (2008) 865.
[20] G. Li, D. Song, Z.P. Li, J. Zhu, Determination of magnetic parameters in La0.7Sr0.3MnO3/SrTiO3 thin films using EMCD, Appl. Phys. Lett. 108 (2016), 242414.
[21] S. Schneider, D. Pohl, S. Löffler, J. Rusz, D. Kasinathan, P. Schattschneider, L. Schultz, B. Rellinghaus, Magnetic properties of single nanomagnets: electron energy-loss magnetic chiral dichroism on FePt nanoparticles, Ultramicroscopy 171 (2016) 186.
[22] S. Muto, K. Tatsumi, J. Rusz, Parameter-free extraction of EMCD from an energy-filtered diffraction datacube using multivariate curve resolution, Ultramicroscopy 125 (2013) 89.
[23] Z.Q. Wang, X.Y. Zhong, R. Yu, Z.Y. Cheng, J. Zhu, Quantitative experimental determination of site-specific magnetic structures by transmitted electrons, Nat. Commun. 4 (2013) 1, 2013 4:1.
[24] Z. Li, et al., Atomic structure and electron magnetic circular dichroism of individual rock salt structure antiphase boundaries in spinel ferrites, Adv. Funct. Mater. 31 (2021), 2008306.
[25] H. Ali, J. Rusz, T. Warnatz, B. Hjörvarsson, K. Leifer, Simultaneous mapping of EMCD signals and crystal orientations in a transmission electron microscope, Sci. Rep. 11 (2021) 2180.
[26] D. Del-Pozo-Bueno, M. Varela, M. Estrader, A. López-Ortega, A.G. Roca, J. Nogués, F. Peiró, S. Estradé, Direct evidence of a graded magnetic interface in bimagnetic core/shell nanoparticles using electron magnetic circular dichroism (EMCD), Nano Lett. 21 (2021) 6923.
[27] K. Xu, T. Lin, Y. Rao, Z. Wang, Q. Yang, H. Zhang, J. Zhu, Direct investigation of the atomic structure and decreased magnetism of antiphase boundaries in garnet, Nat. Commun. 13 (2022) 1, 2022 13:1.
[28] X. Chen, et al., Nanoscale measurement of giant saturation magnetization in α″-Fe16N2 by electron energy-loss magnetic chiral dichroism, Ultramicroscopy 203 (2019) 37.
[29] X. Fu, B. Warot-Fonrose, R. Arras, D. Demaille, M. Eddrief, V. Etgens, V. Serin, Energy-loss magnetic chiral dichroism study of epitaxial MnAs film on GaAs(001), Appl. Phys. Lett. 107 (2015), 062402.
[30] J. Lin, et al., Detection of magnetic circular dichroism in amorphous materials utilizing a single-crystalline overlayer, Phys. Rev. Mater. 1 (2017), 071404.
[31] V. López-Flores, N. Bergeard, V. Halté, C. Stamm, N. Pontius, M. Hehn, E. Otero, E. Beaurepaire, C. Boeglin, Role of critical spin fluctuations in ultrafast demagnetization of transition-metal rare-earth alloys, Phys. Rev. B Condens. Matter Mater. Phys. 87 (2013), 214412.
[32] T. Koide, T. Sekine, H. Miyauchi, H. Manaka, D. Asakura, A. Fujimori, K. I. Kobayashi, Y. Tomioka, T. Kimura, Y. Tokura, Microscopic origin of ferrimagnetism of a double perovskite Sr2FeMoO6: an x-ray magnetic circular dichroism study, J. Phys. Conf. Ser. 502 (2014), 012003.
[33] H. Lidbaum, J.N. Rusz, S. Rubino, A. Liebig, B.H. Orvarsson, P.M. Oppeneer, O. Eriksson, K. Leifer, Reciprocal and real space maps for EMCD experiments, Ultramicroscopy 110 (2010) 1380.
[34] B. Efron, Bootstrap Methods: Another Look at the Jackknife, Ann. Statist. 7 (1979) 1–26.
[35] A. Armigliato, R. Rosa, Simultaneous determination of composition and thickness of thin films by X-ray microanalysis at 300 KV and Monte Carlo simulation, Ultramicroscopy 32 (1990) 127.
[36] D. Choi, X. Liu, P.K. Schelling, K.R. Coffey, K. Barmak, Failure of semiclassical models to describe resistivity of nanometric, polycrystalline tungsten films, J. Appl. Phys. 115 (2014), 104308.
[37] P.A. Penczek, J. Fang, X. Li, Y. Cheng, J. Loerke, C.M.T. Spahn, CTER-rapid estimation of CTF parameters with error assessment, Ultramicroscopy 140 (2014) 9.
[38] T. Thersleff, L. Schönström, C.W. Tai, R. Adam, D.E. Bürgler, C.M. Schneider, S. Muto, J. Rusz, Single-pass STEM-EMCD on a zone axis using a patterned aperture: progress in experimental and data treatment methods, Sci. Rep. 9 (2019) 18170.
[39] P. Schattschneider, M. Stöger-Pollach, S. Rubino, M. Sperl, C. Hurm, J. Zweck, J. Rusz, Detection of magnetic circular dichroism on the two-nanometer scale, Phys. Rev. B Condens. Matter Mater. Phys. 78 (2008), 104413.
[40] J. Salafranca, J. Gazquez, N. Nicolás Pérezpérez, A. Labarta, S.T. Pantelides, S. J. Pennycook, X. Batlle, M. Varela, Surfactant organic molecules restore magnetism in metal-oxide nanoparticle surfaces, Nano Lett. 12 (2012) 54.
[41] T. Thersleff, J. Rusz, S. Rubino, B. Hjörvarsson, Y. Ito, N.J. Zaluzec, K. Leifer, Quantitative analysis of magnetic spin and orbital moments from an oxidized iron (1 1 0) surface using electron magnetic circular dichroism, Sci. Rep. 5 (2015) 13012.
[42] T. Thersleff, S. Muto, M. Werwiński, J. Spiegelberg, Y. Kvashnin, B. Hjörvarsson, O. Eriksson, J. Rusz, K. Leifer, Towards sub-nanometer real-space observation of spin and orbital magnetism at the Fe/MgO interface, Sci. Rep. 7 (2017) 44802.
[43] H. Ali, S.K.M. Sathyanath, C.W. Tai, J. Rusz, T. Uusimaki, B. Hjörvarsson, T. Thersleff, K. Leifer, Single scan STEM-EMCD in 3-beam orientation using a quadruple aperture, Ultramicroscopy 251 (2023), 113760.
[44] M. Bosman, V.J. Keast, Optimizing EELS acquisition, Ultramicroscopy 108 (2008) 837.
[45] D.H. Vincent Hou, Reduce correlated noise in EELS spectrum with high quality dark reference, Microsc. Microanal. 15 (2009) 226.
[46] G.S. Mudholkar, A.D. Hutson, The epsilon–skew–normal distribution for analyzing near-normal data, J. Stat. Plan. Inference 83 (2000) 291.
[47] J. Rusz, S. Rubino, P. Schattschneider, First-principles theory of chiral dichroism in electron microscopy applied to 3D ferromagnets, Phys. Rev. B 75 (2007), 214425.
[48] S. Muto, J. Rusz, K. Tatsumi, R. Adam, S. Arai, V. Kocevski, P.M. Oppeneer, D. E. Bürgler, C.M. Schneider, Quantitative characterization of nanoscale polycrystalline magnets with electron magnetic circular dichroism, Nat. Commun. 5 (2014) 1, 2014 5:1.
[49] B. Warot-Fonrose, C. Gatel, L. Calmels, V. Serin, E. Snoeck, S. Cherifi, Magnetic properties of FeCo alloys measured by energy-loss magnetic chiral dichroism, J. Appl. Phys. 107 (2010) 7.
[50] M. Stöger-Pollach, C.D. Treiber, G.P. Resch, D.A. Keays, I. Ennen, EMCD real space maps of magnetospirillum magnetotacticum, Micron 42 (2011) 456.
[51] A. Rose, in: *The Visual Process , Vision: Human and Electronic*, Springer US, Boston, MA, 1973, pp. 1–27.